Delft University of Technology

SEM-EDX hyperspectral data analysis for the study of soil aggregates

Allegretta, Ignazio; Legrand, Stijn; Alfeld, Matthias; Gattullo, Concetta Eliana; Porfido, Carlo; Spagnuolo, Matteo; Janssens, Koen; Terzano, Roberto

SEM-EDX hyperspectral data analysis for the study of soil aggregates

Ignazio Allegretta [a,*], Stijn Legrand [b,c], Matthias Alfeld [d], Concetta Eliana Gattullo [a], Carlo Porfido [a], Matteo Spagnuolo [a], Koen Janssens [b], Roberto Terzano [a]

[a] Micro X-ray Lab, Dipartimento di Scienze del Suolo, della Pianta e degli Alimenti, Università degli Studi di Bari "Aldo Moro", Via G. Amendola 165/A, 70126 Bari, Italy
[b] AXES Research Group, Department of Chemistry, University of Antwerp, Groenenborgerlaan 171, 2020 Antwerp, Belgium
[c] ARCHES Research Group, Heritage Department, University of Antwerp, Blindestraat 9, 2000 Antwerp, Belgium
[d] Department of Material Science and Engineering, 3ME, TU Delft, Mekelweg 2, 2628CD Delft, the Netherlands

ARTICLE INFO

ABSTRACT

Scanning electron microscopy coupled with microanalysis (SEM-EDX) is an important analytical tool for the morphological and chemical characterization of different types of materials. In many applications, SEM-EDX elemental maps are usually used and processed as images, thus flattening and reducing the spectroscopic information contained in EDX hyperspectral data cubes. The exploitation of the full hyperspectral dataset could be indeed very useful for the study of complex matrices like soil. In order to maximize the information attainable by SEM-EDX data cubes analysis, the software package "Datamuncher Gamma" was implemented and applied to study soil aggregates. By using this approach, different phases (silicates, aluminosilicates, Ca-carbonates, Ca-phosphates, organic matter, iron oxides) inside soil aggregates were successfully identified and segmented. The advantages of this method over the common ROI imaging approach are presented. Finally, this method was used to compare different aggregates in a Cr-polluted soil and understand their possible pedological history. The present method can be used for the analysis of every type of SEM-EDX data cubes, allowing its application to different types of samples and fields of study.

1. Introduction

Scanning electron microscopy (SEM) is an important analytical tool for the micro and nano characterization of many types of samples, and is nowadays widely used in several scientific and industrial fields, from biology to material science (Goldstein et al., 2018). The interaction between the electron beam and the sample produces different types of electrons (i.e. secondary, backscattered and Auger electrons) and photons (i.e. x-rays, visible light) that allow to study the topography, morphology, microstructure and chemical composition of the sample (Goldstein et al., 2018; Wells, 2001). X-rays can be analyzed by either energy dispersive (EDX) or wavelength dispersive (WDX) detectors in order to obtain qualitative and quantitative information about the elemental composition of the sample (Newbury and Ritchie, 2015). The capability of EDX detectors to acquire the full x-ray spectrum emitted by the sample, and the improvement of the signal processing speed, have contributed to develop new analytical strategies capable to acquire data cubes where, at each pixel of a SEM image, an EDX spectrum is

associated. Nevertheless, the technological progress of SEM-EDX instruments has not been followed by the development of adequate software allowing the full exploitation of the information contained in the hyperspectral data cubes. Maps showing the qualitative and quantitative distribution of individual chemical elements are usually created by integrating the number of x-ray photons (counts) recorded in a spectral region of interest (ROI) of the EDX or WDX spectrum over the mapped area. Then, for a given mapped area, correlations between elements as well as identification of phases or features are usually obtained by simply treating the different elemental maps as images, by super imposing a certain number of them according to the preformed hypotheses (Carlton, 2010). Other strategies have been also developed to manage elemental maps. Kenda et al. (1999) applied the concentration histogram image approach to SEM-EDX elemental maps, in order to perform phase analysis on superconducting tapes. Vazquez et al. (2013) converted SEM-EDX maps to binary images and processed them with Boolean operators to evaluate salt crystallization in walls. In all these cases, the use of ROI images may lead to three main problems: i) ROI

---

mapping does not consider the net intensity of the spectrum, meaning that background and overlapping fluorescence lines are not subtracted from the spectrum, resulting in an incorrect or biased presentation of the data; ii) the image preprocessing can alter the map representation, often on a subjective basis, hence affecting the identification of element correlations; iii) the color depth in such files is commonly limited to 8-bit, considerably compressing the dynamic range.

The analytical information contained in the SEM-EDX data cubes can be maximized performing hyperspectral data analysis by spectral deconvolution, which is commonly used for x-ray fluorescence mapping (Allegretta et al., 2016, 2018; Astolfi et al., 2018; Legrand et al., 2019; Porfido et al., 2019; Van der Snickt et al., 2016). A hyperspectral data cube is composed of the pixel position along the x and y axis and the EDX spectrum. Hyperspectral data analysis consists of the processing of all the spectral information via performing a least squares fit of the spectrum to a mathematical model. Conversely, ROI imaging and multi-spectral analysis choose single portions of the spectrum (Germinario et al., 2016). One of the advantages of using hyperspectral data instead of ROI images is that correlations and comparisons between elements are based on objective spectral information rather than on subjectively filtered maps. Despite the hyperspectral dataset of SEM-EDX is similar to that of micro/macro focused x-ray fluorescence (XRF), this approach is not usually applied to SEM-EDX data analysis. To the Authors' knowledge, there are only few cases reported in the literature about phase analysis performed using multivariate statistical analysis on SEM-EDX hyperspectral datasets (Burdet et al., 2015; Kotula et al., 2003). However, these studies were carried out on relatively simple materials (metal-ceramic materials, alloys and particulate), where all the phases have a very different elemental composition. No published work is available on the application of hyperspectral SEM-EDX data analysis of more complex matrices like soil.

The increasing interest for the study and modelling of soil processes at the microscale (Baveye et al., 2018) has led to the development of different analytical strategies combining the microstructural and chemical information obtainable by SEM-EDX, in order to perform soil phase reconstruction (Hapca et al., 2011; 2015; Schlüter et al., 2019). Nevertheless, also in these cases, SEM-EDX chemical maps were extracted as ROI images and part of the spectral information was lost.

In the present work, hyperspectral data analysis by spectral deconvolution is applied to SEM-EDX datasets collected from soil thin sections in order to identify the different soil phases. In particular, the phase analysis was carried out on single soil aggregates containing a complex mixture of organic and inorganic materials. Studying soil aggregates is important for understanding soil properties (Lu et al., 2017) and soil processes, such as pedogenesis (Falsone et al., 2012; Lin, 2011; Zhong et al., 2020) and microbial activity (Rillig et al., 2017; Schlüter et al., 2019), and for studying mobility and stabilization of toxic elements (Cagno et al., 2020; Gattullo et al., 2018, 2020; Li et al., 2020). To investigate the soil samples, "Datamuncher Gamma" software, recently developed to analyse macroscopic x-ray fluorescence scanning datasets (Alfeld and Janssens, 2015) and already used to study soil thin sections by μXRF (Allegretta et al., 2018; Gattullo et al., 2018, 2020), was adapted to analyse the SEM-EDX data cubes by spectral deconvolution. Results obtained were compared with ROI imaging, which is the standard procedure for SEM-EDX mapping. The proposed approach allowed the segmentation and quantification of different phases in a single soil aggregate, as well as the comparison of different aggregates within a Cr-polluted soil sample. This methodology ultimately enabled the study of microstructural features and identification of the origin of soil pollution and related processes.

2. Materials and methods

2.1. Soil characteristics and sample preparation

Soil samples were collected at 0–20 cm depth from an agricultural

site near the town of Altamura (Bari, Southern Italy). The soil is silt loam with a high content of organic matter (234 g/kg) and a weakly alkaline pH (7.5). Calcium, Al, Si, Fe, K, P and S are the major elements detected in the soil. The investigated soil shows also a very high concentration of Cr (5160 mg/kg), as a consequence of amendment with tannery waste-derived material, as reported by Gattullo et al. (2020). From a mineralogical point of view, it is characterized mainly by the presence of calcite, illite, kaolinite, plagioclase and quartz. Further information on the soil characteristics is available in Gattullo et al. (2020).

The soil was air dried, sieved at 2 mm and impregnated under vacuum with an epoxy resin (L.R. White Resin, Polyscience Europe GmbH, Germany). Then, the resin-embedded sample (20×30 mm^2) was cut, glued to a glass slide and lapped in a first step with a silicon carbide paste, and then with a diamond paste to reach a thickness of 32 μm. Finally, the thin section was carbon coated using a sputter coater.

2.2. SEM-EDX analyses

Analyses were carried out with a field emission gun scanning electron microscope (FEG-SEM, Zeiss Σigma SUPRA 300 VP, Carl Zeiss NTS GmbH, Germany), equipped with a backscattered electron detector (BSED) and an EDX C-MaxN SDD spectrometer with an active area of 20 mm^2 (Oxford Instruments, England). Analyses were performed using a working distance of 7.5 mm, an aperture of 60 μm and a beam voltage of 15 kV. The acquisition time and dwell time were set at 5 s/cycle and 100 μs/px, respectively. In order to identify the best acquisition conditions, chemical maps were acquired using 100, 200, 500 and 1000 cycles (corresponding to a total acquisition time of 8, 16, 33 and 67 min, respectively), and calculating the signal-to-noise ratio (S/N) for each detected element according to Ernst et al. (2014).

For the phase identification, point analyses were performed on the segmented features. Point analyses were measured for 60 s using the same working distance, aperture and beam tension reported above. Three points per recognized phase were analyzed.

2.3. Standard method for SEM-EDX mapping: ROI imaging

After the collection of SEM-EDX data cubes, the region of interest (ROI) of each element was identified. A ROI is the portion of the EDX spectrum containing the most intense characteristic emission line of an element (usually K-alpha lines). The element distribution maps were produced displaying the number of photon counts of the element ROI in each pixel of the image. Binary scatterplots based on the photon counts recorded for the characteristic ROIs of two selected elements were produced to find the correlations between elements and identify the soil phases.

2.4. Hyperspectral data analysis by spectral deconvolution with Datamuncher Gamma

A hyperspectral data cube has two lateral and one spectral dimensions, with several hundreds to thousands of entries in each dimension. Compressing these data sets into an easily legible graphical representation is required for an interpretation of the acquired data.

The process underlying how the shape of a peak forms in a spectrum is well understood and can be mathematically modelled (Van Espen, 2002). Each peak can be approximated with a Gaussian like shape, and can be described by three parameters: position of its maximum, width and area. The energy resolution of a detector is dependent on the energy of the detected photon. The relative peak position is known from the energy of fluorescence lines in spectral libraries. Consequently, a mathematical model can be built using the detector calibration and response function as non-linear parameters, and the peak areas as linear dependent parameters. This model can be fitted to a spectrum to calculate the non-linear parameters and the peak areas. The continuum under the peaks can be addressed either as a polynomial function in the

model or by filtering the spectrum before. The area of such a peak approximates the number of photons detected for the given fluorescence lines, and can be used for the calculation of elemental distribution images.

The non-linear parameters can be determined by fitting the model to a spectrum. Doing this for each spectrum of the dataset is possible but not recommended, as the non-linear parameters related to the detector are expected to be constant throughout the scan. Further, as the statistics of individual spectra are limited, the uncertainty of the yielded non-linear parameters would also be relevant. Another possibility is to determine all non-linear parameters on a sum spectrum of all pixels, and then fit each spectrum of the data set with the non-linear parameters set to fixed values. This method is essentially a linear regression of the spectrum with pre-determined peak profiles. The two approaches described are currently based on matrix multiplication ("Dynamic Analysis"), developed for GeoPIXE (Ryan and Jamieson, 1993) and implemented in Datamuncher Gamma (Alfeld and Janssens, 2015), or the usage of non-negative least squares fitting, as in PyMCA (Solé et al., 2007).

Independently from the method used, the acquired elemental information commonly has a dynamic range beyond the classical 8-bit limit of greyscale images, so that information is lost if it is directly transferred into such an image. In order to highlight the relevant features and obtain legible images, it is recommended to interpret the yielded data without compression in a dedicated computer program and carefully select the conversion into 8-bit greyscale. This was one of the concepts behind the development of Datamuncher Gamma. The software was written in the Interactive Data Language (IDL) and was published on sourceforge (https://sourceforge.net/projects/datamuncher/).

The processing of the datasets starts with the calculation of sum and maximum pixel spectra in Datamuncher. The sum spectrum is obtained by summing up all the EDX spectra acquired in each single pixel of the map, and the maximum pixel spectrum features the maximum intensity of each channel recorded anywhere in the map. The sum spectrum is fitted with a non-negative least squares fitting model by using the software PyMCA (Solé et al., 2007). The maximum pixel spectrum is used to identify elements that are encountered only in few points of the sample surface. Then, the obtained elemental profiles are imported in "Datamuncher Gamma" to perform the fitting of the spectrum contained in each pixel of the map, using the average spectral background to describe the background in individual spectra. Based on the fitted spectra, a new spectral data cube is created, which contains the net intensities of the element fluorescence lines in each pixel. Further information on

Datamuncher can be found in Alfeld and Janssens (2015).

2.5. Applications of SEM-EDX analysis

The first part of this work dealt with the identification of different phases and features inside a soil aggregate (Fig. 1A), chosen because of its very complex microstructure. More specifically, this aggregate was characterized by several inclusions and a matrix composed of two regions of different color and, hence, composition (the two regions are separated by a red dashed line in Fig. 1A). Such complex aggregate allowed to determine the optimal acquisition conditions and evaluate the performance of the analysis. In order to perform the phase analysis, scatterplots based on the fitted net-intensities of two different elemental lines (i.e., two elements) were considered, and existing correlations (e.g. belonging to different minerals or soil features) were visually projected by the software on the sample surface image. The segmentation and quantification of the different phases was performed with JMicroVision v1.2.7 (Roduit, 2007).

Furthermore, SEM-EDX hyperspectral data analysis was performed on 18 different aggregates of a Cr-polluted soil, having a size between 500 and 2000 μm. They were chosen in order to have specimens representative of different microstructures which could be related to different origins or pedological histories. To compare the data acquired on the different soil aggregates, the 18 fitted net-intensity data cubes were merged and elements correlations were found.

3. Results and discussion

3.1. Determination of optimal data acquisition conditions

The best data acquisition conditions were selected based on the quality of the EDX spectrum collected on the soil aggregate shown in Fig. 1A. In particular, the signal-to-noise ratio (S/N) for each element detected in the aggregate was monitored. This parameter usually improves by increasing the acquisition time and, in fact, the quality of the EDX spectrum improved by increasing the number of acquisition cycles. The sum spectra obtained with the four different conditions (100, 200, 500 and 1000 cycles) are reported in Fig. 1B. These spectra reveal the presence of the K-lines of C, O, Na, Mg, Al, Si, P, S, Cl, K, Ca, Ti, Cr, Mn and Fe and the L-lines of Fe. Looking at Fig. 1B, Cr-Kα and Mn-Kα peaks are very weak in all the four sum spectra. Since this soil is characterized by Cr-pollution (Gattullo et al., 2020), a particular attention was given to the S/N of Cr-Kα. This parameter increased with the number of cycles
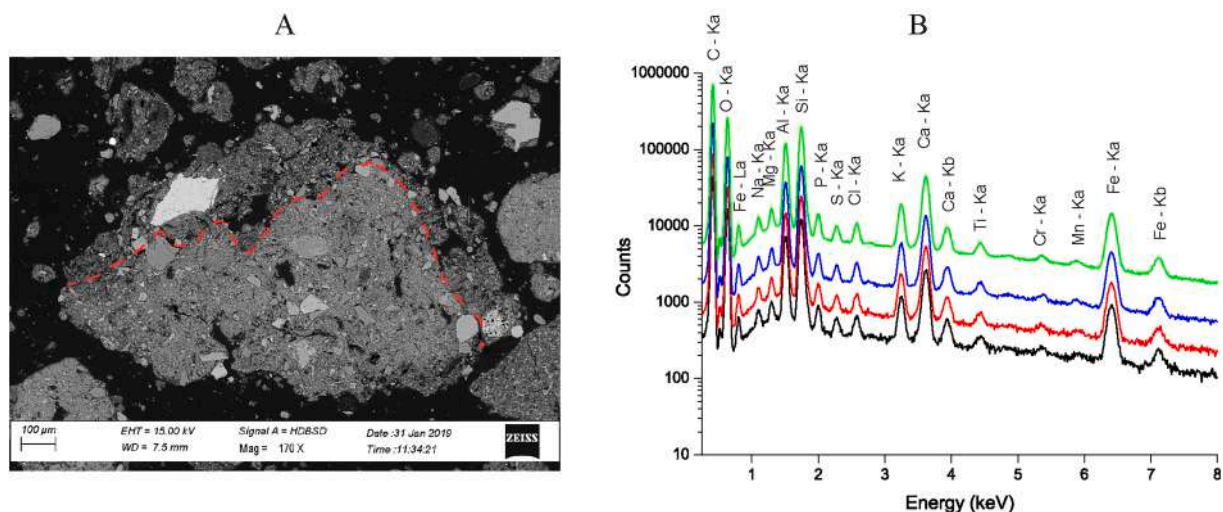

Fig. 1. Backscattered micrograph of a soil aggregate in a thin section (A) and EDX sum spectra (B) of the four maps acquired on the same aggregate after 100 (black), 200 (red), 500 (blue) and 1000 (green) cycles. The red dashed line shows the separation between two different regions in the aggregate.

and accounted to 8, 9, 14 and 25 using 100, 200, 500 and 1000 cycles, respectively. An $S/N \geq 3$ is sufficient for qualitative analyses, while an $S/N \geq 10$ should be achieved for semiquantitative and quantitative analyses. In fact, at $S/N = 10$ a theoretical uncertainty of 30% is still associated to the element quantification at 99.7% of confidence level (Ernst et al., 2014). Since an accurate quantitative analysis was not the purpose of this study and phase identification needs reliable intensities of the fluorescence peaks, 500 cycles were considered sufficient, as they allowed an $S/N \geq 10$ for most of the elements. In the case of Mn, the S/N was always lower than 10 (reaching a level of 7 after 1000 acquisition cycles). This was due to the low Mn concentration in the sample (<800 ppm). The use of 500 acquisition cycles allowed to obtain an $S/N = 4$ for Mn, which was considered sufficient since identification of Mn-bearing phases was not relevant for this study.

3.2. Phase analysis on single soil aggregate

3.2.1. Comparison of elemental maps

The backscattered electron (BSE) micrograph reported in Fig. 1A shows the complex microstructure of the studied soil aggregate. The brighter objects are associated with denser phases, while the darker parts are attributable to less dense materials, like soil organic matter and the epoxy resin that surrounds the aggregate and fills the pores. For each element detected in the sum spectrum (Fig. 1B), elemental maps were produced using both the full spectral deconvolution approach with Datamuncher Gamma and ROI mapping (Fig. S1). In order to compare the elemental maps obtained with the two methods, the number of counts was scaled for each element. As a first evidence, SEM-EDX maps produced after spectral deconvolution (SD, Fig. S1) appear brighter than ROI maps (ROI, Fig. S1). In fact, with spectral deconvolution, a 20% higher number of counts were recorded in each pixel respect to ROIs. With the use of ROIs, only the photons recorded at the main EDX line of the element within a narrow window of channels are considered while, with spectral fitting, the whole peak is integrated (Fig. S2). Moreover, just one line per element is considered using ROIs, while more lines are fitted with performing the spectral deconvolution (e.g. Kα and Kβ of K, Ca and Ti in Fig. S2). Finally, using ROIs it is not possible to discriminate among overlapping peaks (for instance, the overlapping of K-Kβ and Ca-Kα shown in Fig. S2), as well as to detect and subtract other spectral contributions (i.e. bremsstrahlung continuum and detector artefacts, such as escape or pile-up peaks). Nevertheless, the refined ROI imaging can be implemented to include corrections for the continuum intensity at the edge of ROI. Moreover, spectral overlapping of the signals of different elements may be partially resolved by digitally subtracting the distribution images of different elements from one another. This procedure has some drawbacks, as it requires data manipulation, is partly subjective and the subtraction of ROI images may result in noise enhancement.

For the most concentrated elements, both the data elaborations allow the identification of two regions in the aggregate: a core part with a relatively high O, Si and Al signals (below the red dashed line in the BSE micrograph of Fig. 1A), and a border part (above the red dashed line) where their intensity is much lower (Fig. S1). The difference in brightness of these two regions could be ascribed to two main reasons: a real decrease in O, Al and Si concentration in the border portion, or an increased porosity (i.e., a lower total amount of these elements per unit volume). The increase of the C signal in the border part can be attributed to both an increase in organic matter and the presence of epoxy resin filling the pores of the aggregate.

For the less concentrated elements (such as Na, Mg, K, Cr and Fe), the spectral fitting allows to identify more regions where the element is present. This is especially the case of K, where further bright pixels are visible after the spectral fitting (Fig. S1) revealing the presence of this element both in small domains, with high K concentration, and in the aggregate matrix. Some more intense spots can be seen also in the Na, Mg and Ca maps after spectral deconvolution. The use of spectral

deconvolution also allows to improve the information about Fe in the whole aggregate matrix, and Cr in the small domain at the bottom part of the map. However, looking just at Fig. S1, both ROI images and elemental maps after spectral deconvolution do not allow the identification of different phases in the aggregate. Only in one case, the strong overlapping of Ca and P maps clearly suggests the presence of calcium phosphate phases.

3.2.2. Phase identification using elements correlations

Another approach, based on the comparison of the net fluorescence signal intensity of two different elements, was useful to recognize additional features and to identify different phases within the aggregate. By using spectral deconvolution data, the C vs O scatterplot reported in Fig. 2A discriminates three different regions in the micrograph with different C/O signal ratios: (i) the resin both inside (in pores) and outside the aggregate (in blue, with a high C content), (ii) the border portion of the aggregate (in green, as already recognized in the BSE micrograph in Fig. 1A), and (iii) the C-poor inner part of the aggregate (in red). Hapca et al. (2015) suggested that once soil is analyzed as thin section with SEM-EDX, resin and organic matter can be segmented based on the C/O ratio. However, segmentation becomes more difficult if the sample contains large amounts of calcium carbonate, as in the soil under investigation, which contains 17% of calcite (Gattullo et al., 2020). Indeed, the points of the map having a green-labelled C/O ratio are also characterized by an intense Ca signal (Fig. S1), thus suggesting the occurrence of Ca-carbonate. In order to discriminate between organic matter and Ca-carbonate, the C vs Ca scatterplot was considered (Fig. 2B). The latter allowed to distinguish a portion with a high Ca/C ration (in red), ascribable to Ca-carbonates and phosphates, and a portion (in white) attributable to organic matter. The strong correlation between Ca and C in the organic fraction of this soil is due to soil amendment with tannery sludge, which typically contain large amounts of Ca (deriving from the leather liming process) besides organic material from leather residues (Gattullo et al., 2020; Silva et al. 2014). Identifying organic matter in soil aggregates is very important since it strongly affects the soil physical–chemical properties, such as the structure, porosity, and cation exchange capacity. The preliminary determination of calcium carbonate content in soil can thus help to correctly segment the organic matter areas based on SEM-EDX data cubes.

The Al vs Si scatterplot (Fig. S3) shows the presence of four different pixel groups with different Al/Si ratios: the aggregate matrix (in red), two regions with high (green) and low (pink) Al content, and a region belonging to silicates, where no Al is detected (blue).

The correlation maps are very useful to obtain a general idea of the composition of the aggregate. To improve the quality of the phase analysis, the emission signals from additional elements were considered. A discrimination of silicates and aluminosilicates was performed by comparing the EDX signals of Si, Al, K, Na, Mg and Ca (Fig. 3). Table 1 reports the results of point analyses for each of the phases identified in Fig. 3.

The Si-rich domains shown in Fig. 3A (in pink) correspond to quartz, since they contain only Si and O (Table 1). Feldspars and plagioclase were identified using the Al vs K (Fig. 3B) and Na vs Si (Fig. 3C) scatterplots, respectively. No overlapping was found between the K-feldspar (in red) and Na-plagioclase (in blue) domains. Chemical composition by microanalysis (Table 1) confirmed the two phases and excluded the co-presence of K and Na in the feldspar and that of Na and Ca in the plagioclase. The combination of these two areas (labelled red and blue) overlaps perfectly with the green-labelled area in Fig. S3, meaning that almost all the aluminosilicate phases were identified. A correlation between the EDX signals of Mg and Si was found (in green, Fig. 3D), but not between those of Mg and Al (data not shown). The same green-labelled areas could be identified in the scatterplot of Ca vs Si (in green, Fig. 3E). The chemical point analysis reveals a very low concentration of Al in these areas, thus explaining the correspondence between the green-labelled areas in Fig. 3D and the pink domains in Fig. S3. The
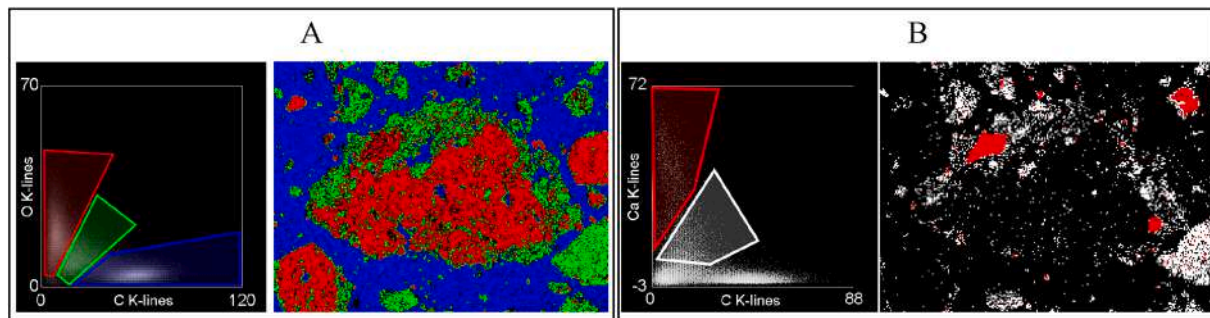
Fig. 2. C vs O scatterplot and relative false-color map, revealing the presence of three C/O ratios belonging to the matrix of the aggregate (red), the resin (blue) and organic matter/Ca-carbonates (green) (A). C vs Ca scatterplot and relative false-color map revealing the presence of two Ca/C ratios belonging to Ca-carbonates and phosphates (red) and organic matter (white) (B). The fitted net EDX intensities in the scatter biplots are expressed in counts.

chemical composition of these domains can be ascribed to an alumino-silicate of Mg and Ca, probably juanite ($Ca_{10}Mg_4Al_2Si_{11}O_{39}\cdot4H_2O$). Ca-rich domains are also found both inside and outside the soil aggregate (cyan, Fig. 3E). Ca-rich domains can be ascribed both to carbonates and phosphates, and Ca/C ratio cannot help in their discrimination (Fig. 2B). Nevertheless, the Ca vs P scatterplot clearly points out the phosphate domains in the aggregate (yellow, Fig. 3F). For this reason, the Ca-carbonate domains can be obtained simply by subtracting the yellow-labelled phosphate areas from the cyan-labelled ones. Finally, Fe and Si EDX signals were compared (Fig. 3G) and, excluding the Si-rich domains, two additional groups were found: a Fe-rich domain associated to iron oxides and/or hydroxides (orange), and a domain showing the co-presence of Si and Fe, mainly associated to the matrix of the aggregate (grey). All these pieces of information allowed the final segmentation of the different phases present in the soil aggregate. Such final segmentation, representing a phase model of the soil aggregate (Fig. 4), was obtained by first performing a thresholding on the BSE micrograph to isolate the entire aggregate from the background (Fig. 3H), and then by over imposing all the domains identified by the scatterplot correlations on the aggregate shadow. Organic matter and pores were also included in the model, and labelled in white and gray, respectively. By performing image analysis on the phase model obtained, quantitative results for the recognized phases could also be derived (Table 2). The largest part of the aggregate is represented by the matrix (70.4 %) which is mainly composed of a mixture of clay minerals (such as illite and kaolinite), as well as cryptocrystalline and amorphous phases (Gattullo et al., 2020). Quartz (3.7 %), K-feldspar (3.1 %), plagioclase (3.1 %) and CaMg-aluminosilicate (0.8 %) are mainly present in the core part of the aggregate, while organic matter (7.0 %), Ca-carbonates (1.3 %), Ca-phosphates (4.9 %) and Fe-oxides (1.9 %) are mainly located in the border part. The porosity is about 3.7 %. Excluding the Ca-phosphates (for which only one large particle was identified), all the other phases have a median equivalent circle diameter (ECD) comprised between 15 and 20 μm. The maximum ECD is in the range 49–90 μm, while the minimum ECD ranges between 12 and 14 μm.

For comparison, phase identification was also performed using the ROI maps of the detected elements, as usually done in standard SEM-EDX analysis. The ROI of O, Al, Si, P, Na, Mg, K, Ca and Fe were considered and scatterplots comparing two elements are shown in Fig. S4. The clouds of points in the scatterplots (Fig. S4) do not allow the identification of all the phases recognized after performing spectra deconvolution. Some correlations were found between Si and Na (Fig. S4C), Si and Mg (Fig. S4E), Si and Ca (Fig. S4F), and Ca and P (Fig. S4G). These led to the identification of some phases like plagio-clases, CaMg-aluminosilicates and Ca-phosphates but no other phases can be recognized. K-feldspars cannot be identified since no correlation between K and Al was found (Fig. S4D). This comparison clearly shows the advantage of applying spectral deconvolution rather than simple ROI for phase identification using SEM-EDX data. This approach can be

used to provide the chemical and/or mineralogical information required for the chemical modelling of the soil (Hapca et al., 2011; 2015; Schlüter et al., 2019). However, depending on the scale at which a 3D-model should be developed, different kind of thin sectioning could be used in order to obtain a good correspondence between microstructural data (usually X-ray computed tomography dataset) and the results of the phase analysis. Alternatively, for modelling the soil at the sub-micrometer and nanometer scale, another and more precise soil sectioning procedure, such as focused ion beam (FIB), should be used (Gerke et al., 2021).

3.3. Comparison of different soil aggregates

Soil aggregates microstructure and composition affect the physical, chemical and biological properties of the soil and, therefore, soil functioning. The aggregate microstructure and composition can change according to events and reactions taking place during pedogenesis, as well as a consequence of anthropic activities such as agricultural practices (Chadwick and Chorover 2001; Falsone et al 2012; Lin 2011). The analysis of aggregate microstructure is therefore extremely important to assess the impact on soil structure of agricultural practices, such as tillage, cover cropping, green manuring, or soil amendments other than to study the soil–plant-microorganism interactions occurring in the rhizosphere. This analytical approach could also be useful to investigate the origin of adverse anthropic effects on soil, including soil pollution. In this perspective, the chemical information obtained by SEM-EDX hyperspectral data analysis can be very useful to identify, in a polluted soil, the aggregates of anthropogenic origin (deriving, for instance, from the disposal of wastes or contaminated matrices on soil), and to make hypotheses on the origin and source of pollution. As an example of this application, the analysis of selected 18 representative aggregates of a heavily Cr-polluted soil collected in the South of Italy (Gattullo et al., 2020) is reported. The related BSD micrographs of the aggregates are shown in Fig. S5.

The microstructure analysis revealed that all the aggregates show a uniform matrix, excluding P15 where a darker border is observed (see also section 3.2.1), and P16, characterized by a brighter region on the top-right portion. Some aggregates show cracks (P01) or fractures (P06, P07, P10, P12, P13 and P14) probably due to swelling and shrinkage produced by water fluctuations, or contain subrounded pores (P05, P16, P17 and P18). Mineral inclusions were observed almost in all the aggregates (brighter areas). Beside these visual differences, a further differentiation of the aggregates can be done based on the chemical data. In particular, the matrix of the different aggregates can be compared and distinguished based on its chemical composition. The C vs O scatterplot (Fig. 5) allowed performing a first discrimination of the different aggregate matrices.

Excluding the blue-labelled areas with low O content (resin in Fig. 5), which evidence the presence of cracks, fractures and large pores, two
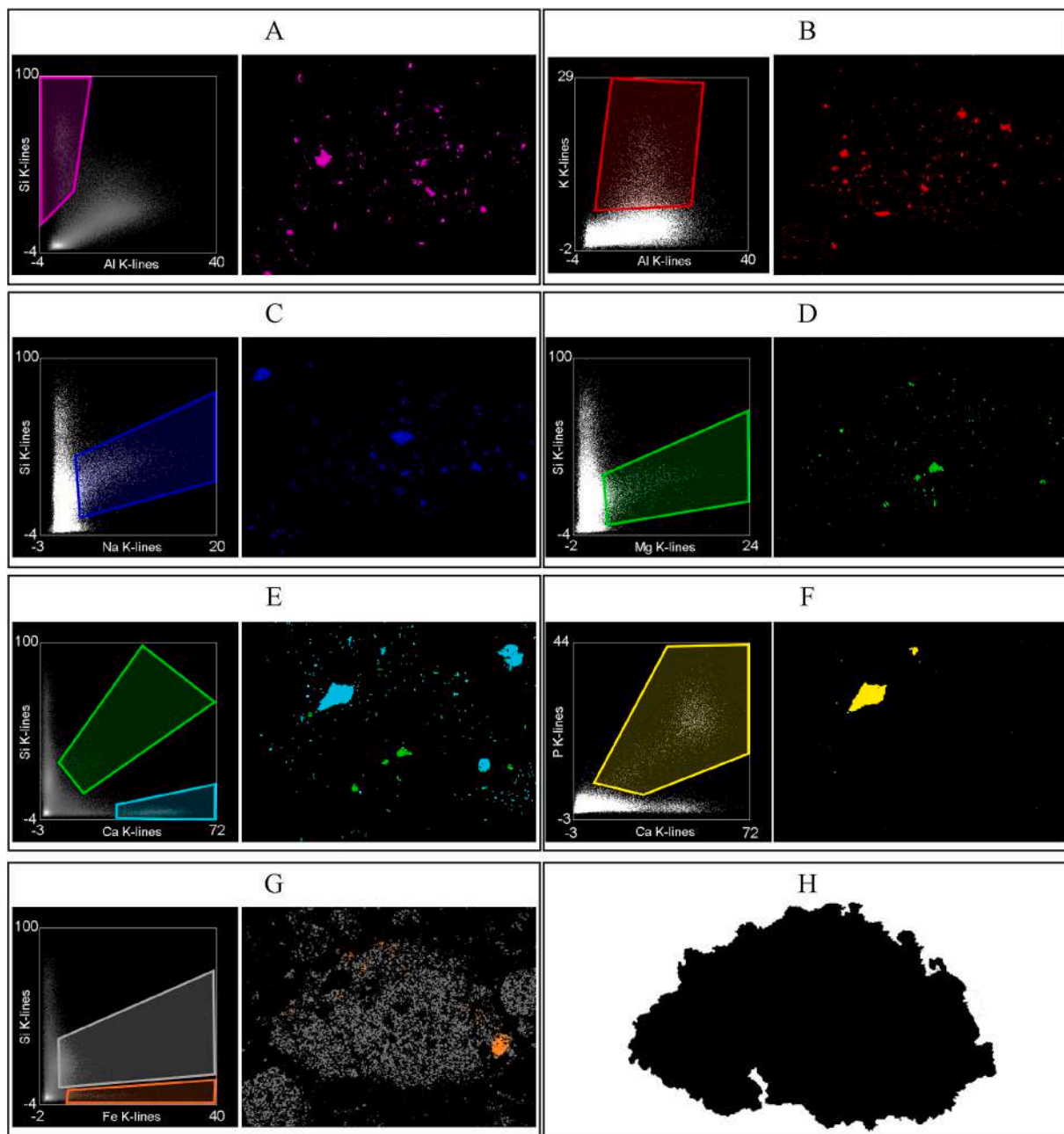
Fig. 3. Identification of different phases inside the soil aggregate: quartz (A, pink), K-feldspars (B, red), plagioclase (C, blue,), CaMg aluminosilicate (D and E, green), Ca-carbonates (E, cyan), Ca-phosphates (F, yellow), Fe oxides (orange) and matrix (G, grey). The aggregate shadow was segmented from the BSD micrograph (H). The fitted net EDX intensities in the scatter biplots are expressed in counts.

different matrices could be distinguished: i) an organic based matrix (green) with an intermediate C/O ratio, and ii) an inorganic matrix (red) where C concentration is very low. Aggregates P15 and P18, characterized by an inorganic matrix, are surrounded by a green-labelled layer (organic layer), while in the case of P16 a rounded organic grain (green) is visible in the upper-right portion of the aggregate.

The Al vs Si scatterplot (Fig. 6) further allows to highlight the differences between the two matrices, showing that the inorganic matrix (P11, P15-P18) is mainly composed of aluminosilicates (yellow). Observing the aggregates from P01 to P10 and from P12 to P14, it is evident that a thin aluminosilicate layer covers the border of the organic matrix. This evidence suggested that aluminosilicate materials with a composition similar to the matrix of inorganic aggregates (P11, P15-P18) possibly deposited over time on the organic aggregates. It is interesting to notice that Cr K-lines were observed only in the aggregates

characterized by an organic matrix. This behavior was associated to the cause of the soil pollution, as already evidenced by Gattullo et al. (2020) using µXRF hyperspectral data analysis on the same soil.

However, some differences can be observed among all the organic aggregates based on their Cr content. Fig. 7 shows the differences among the aggregates based on the Fe vs Cr scatterplot.

In conclusion, five different types of aggregates were recognized:

Group I: P11, P15, P16, P17 and P18 - Aggregates with an aluminosilicate matrix (yellow-labelled Al/Si ratio in Fig. 6) with no Cr in the matrix (blue-labelled Fe/Cr ratio in Fig. 7). This type of aggregates shows a uniform matrix containing angular-subangular mineral inclusions and subrounded pores. An organic rounded area is also visible at the top-right part of P16, but it cannot be considered part of the aggregate as the shape and position suggest.

Group II: P06, P07, P10, P12, P13 and P14 - Aggregates with an

Table 1
Elements concentrations in the coloured areas of Fig. 3 (pink, red, blue, green, cyan, yellow and orange) and Fig. 4 (white and black) as identified by the phase analysis.

Element	Pink Mean	SD*	Red Mean	SD	Blue Mean	SD	Green Mean	SD	Cyan Mean	SD	Yellow Mean	SD	Orange Mean	SD	White Mean	SD	Black Mean	SD
	wt. %																	
O	51.5	1.6	45.1	3.0	54.1	2.1	45.2	2.2	44.3	1.7	37.4	4.5	25.5	20.1	28.9	2.5	50.5	2.8
Al			9.9	0.2	9.6	0.1	3.1	0.5							2.1	1.0	15.3	2.1
Si	48.5	1.6	29.7	0.7	27.3	2.4	23.2	0.3							2.6	1.3	22.3	2.7
Na			0.3	<0.1	8.4	0.1											0.6	0.5
K			15.1	2.6											0.3	0.2	2.8	0.7
Mg							8.2	0.7									0.9	0.6
Ca					0.5	0.5	20.4	2.0	43.7	1.7	43.2	4.5			6.4	2.4	2.3	0.7
Cr															0.5	0.1		
Fe													73.8	20.8	3.0	1.3	5.4	1.4
P											17.0	<0.1						
S													0.7	0.7	1.0	0.3		
F											2.5	<0.1						
C									12.0**	–					56.4	3.0		

* SD = standard deviation
** Value taken from www.webmineral.com
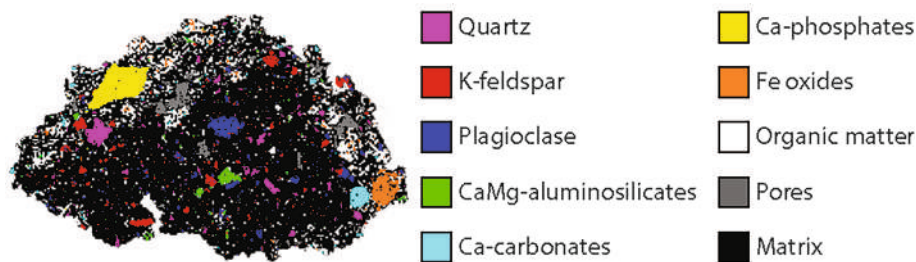
Fig. 4. Aggregate reconstruction on the basis of the elements' correlations shown in Fig. 2 and Fig. 3. The phases represented are: quartz (pink), K-feldspars (red), plagioclase (blue), CaMg-aluminosilicate (green), Ca-carbonates (cyan), Ca-phosphates (yellow), Fe oxides (orange), organic matrix (white), pores (grey) and matrix (black).

Table 2
Volume percentage and particle dimension expressed as equivalent circle diameter (ECD) calculated for each segmented phase obtained after the fitting.

	Quartz	K-Feldspar	Plagioclase	CaMg-aluminosilicate	Ca-phosphates*	Ca-carbonates	Fe-oxides	Organic matter	Pores	Matrix
Volume (%)	3.7	3.1	3.1	0.8	4.9	1.3	1.9	7.0	3.7	70.4
ECD Median (μm)	17	17	16	18	160	15	20	17	17	–
ECD Max (μm)	84	49	90	56	160	71	94	51	61	–
ECD Min (μm)	12	12	12	13	160	12	15	12	12	–

* Only one feature was detected in the soil aggregate.

organic matrix having a high Cr/Fe ratio (labelled in red in Fig. 7). These aggregates have a fractured matrix containing subangular mineral inclusions (Fig. S5).

Group III: P03 and P04 - Aggregates with an organic matrix and spotted areas of high Cr/Fe ratio (Fig. 7) evidencing the presence of small hotspots of Cr and a heterogeneous distribution of the pollutant. They are characterized by a uniform matrix and do not contain inclusions.

Group IV: P05, P08 and P09 - Aggregates with an organic matrix showing a medium Cr/Fe ratio (green in Fig. 7). They have an elliptical shape and contain subrounded mineral inclusions and pores that orientate along the major axis of the aggregate (Fig. S5). Some areas in the inner part of the aggregates show a high Cr/Fe ratio.

Group V: P01 and P02 - Aggregates with an organic matrix and a low Cr/Fe ratio. Different portions of these aggregates belong either to the green or blue-labelled groups (Fig. 7). Their matrix has a uniform microstructure characterized by cracks produced by swelling-shrinkage phenomena.

The first group of aggregates (aluminosilicate matrix) was found also in an adjacent non-polluted soil that was used as control sample in a previous study (Gattullo et al., 2020). For this reason, these Cr-free

aggregates could be considered as autochthone soil aggregates, present in soil before the pollution events. Conversely, the other aggregates should be considered allochthones, since Cr-containing aggregates were not found in the control sample. The differences among the four types of Cr-bearing aggregates could be imputed to three main reasons: i) disposal on the soil of different types of Cr-containing wastes (i.e., tannery byproducts, sewage sludge, chromite-ore processing residues and many others), or ii) disposal of the same type of wastes (for instance, tannery sludge) differently treated according to production process and origin (for instance, wastes deriving from different companies), or (iii) disposal of wastes at different times. The fact that all these aggregates contain large amounts of organic matter (Fig. 5) suggests that their possible provenance is the leather industry, since tannery wastes contain from 65% to 90% of organic matter (Fela et al., 2011). Moreover, small intact leather residues were found in some of the aggregates (Gattullo et al., 2020). During the leather production cycle and wastewaters treatment, sludge having different Cr/Fe ratio can be produced owing to the addition of different kinds of flocculants, such as ferric chloride (Ozgunay et al. 2007). This would explain the different Cr/Fe ratio observed in the aggregates. Tannery wastes are also rich in water (up to 50–60%) and its loss could be the cause of the cracking of the aggregates
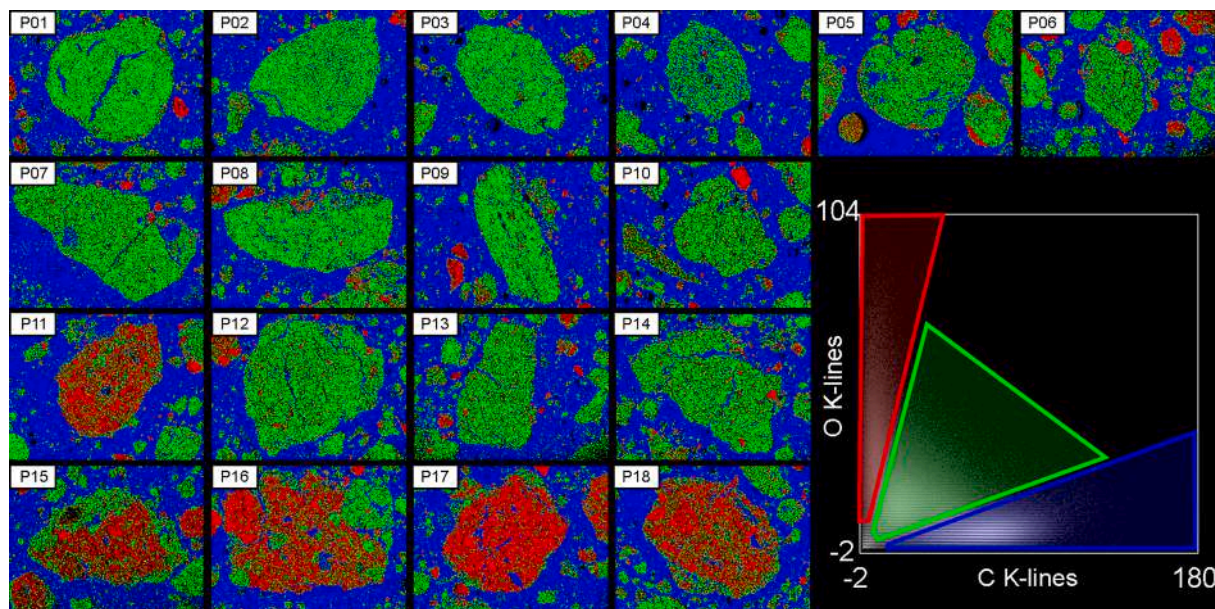
Fig. 5. Identification of three different regions on the base of C vs O scatterplot (right graph) and their visualization in the studied soil aggregates (small panels). The net EDX intensities in the scatter biplots are expressed in counts.
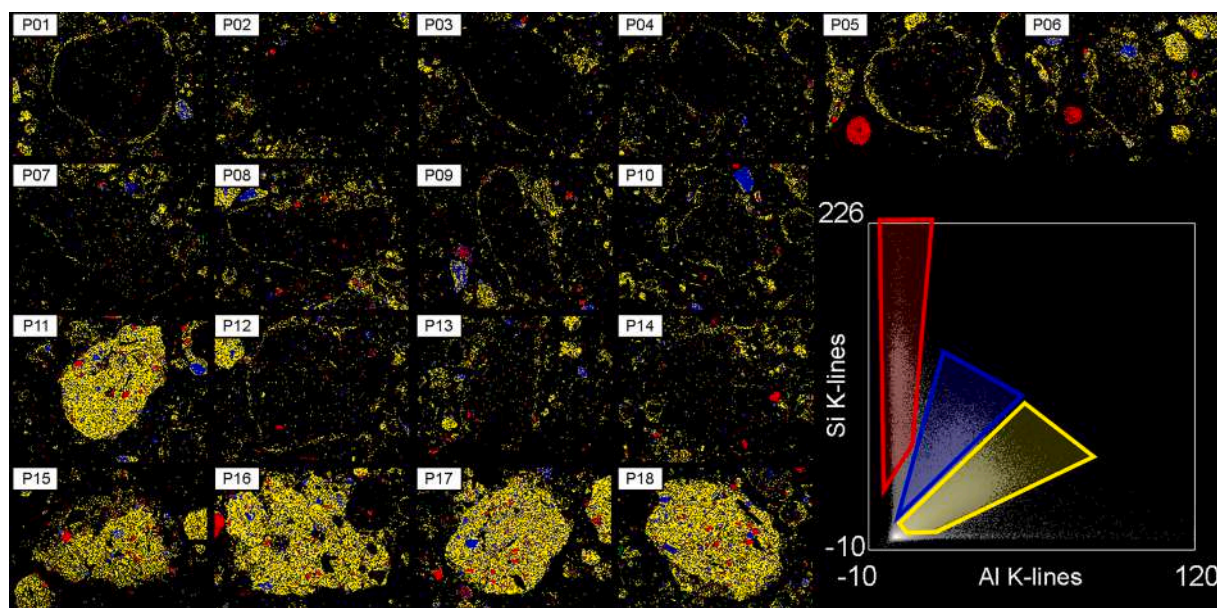

Fig. 6. Identification of three different regions on the basis of Al vs Si scatterplot (right graph) and their visualization in the studied soil aggregates (small panels). The fitted net EDX intensities in the scatter biplots are expressed in counts.

(Fela et al., 2011). Some hypotheses can be done based on the Cr vs Fe biplot (Fig. 7). Fe^{2+} solutions are often used for the treatment of tannery wastes in order to reduce Cr(VI) to Cr(III) (Kannaujiya et al., 2019). Aggregates of group IV and V, which have a medium and low Cr/Fe ratio, could result from a stabilization process with Fe^{2+} solutions. Probably, the same process was not applied (or not to the same extent) to the aggregates of group II, as proved by the very high Cr/Fe ratio. However, aggregates of group IV and V are rounded or elliptical, meaning that they probably underwent a mixing/mingling process differently from the aggregates of group II, which have sharp boundaries. Aggregates of group III have just some spots of high Cr/Fe ratio, meaning that they are probably organic matter particles adsorbing Cr, due to the high binding affinity of organic matter for Cr(III) (Tokunaga et al., 2003; Tokunaga et al., 2001).

The same conclusions cannot be drawn with the use of simple ROI images. In fact, the comparison of Cr and Fe signal in the 18 aggregates (Fig. S6) shows a different grouping. In particular, aggregates previously belonging to group II and IV show now the same Cr/Fe ratio (red). The zoning of P09 (visible in Fig. 7) is also lost. Additionally, the C vs O biplot does not give information about the matrix since organic and aluminosilicate aggregates show the same C/O ratio (red), even if the density of red points is higher in aluminosilicate aggregates than in organic ones (Fig. S7). On the contrary, Al vs Si scatterplot (Fig. S8) discriminates between organic and aluminosilicate aggregates even if the region of the scatterplot connected with the matrix of group I aggregates (yellow) is more spread than the one in Fig. 6, and the information about the third Al/Si ratio is lost.

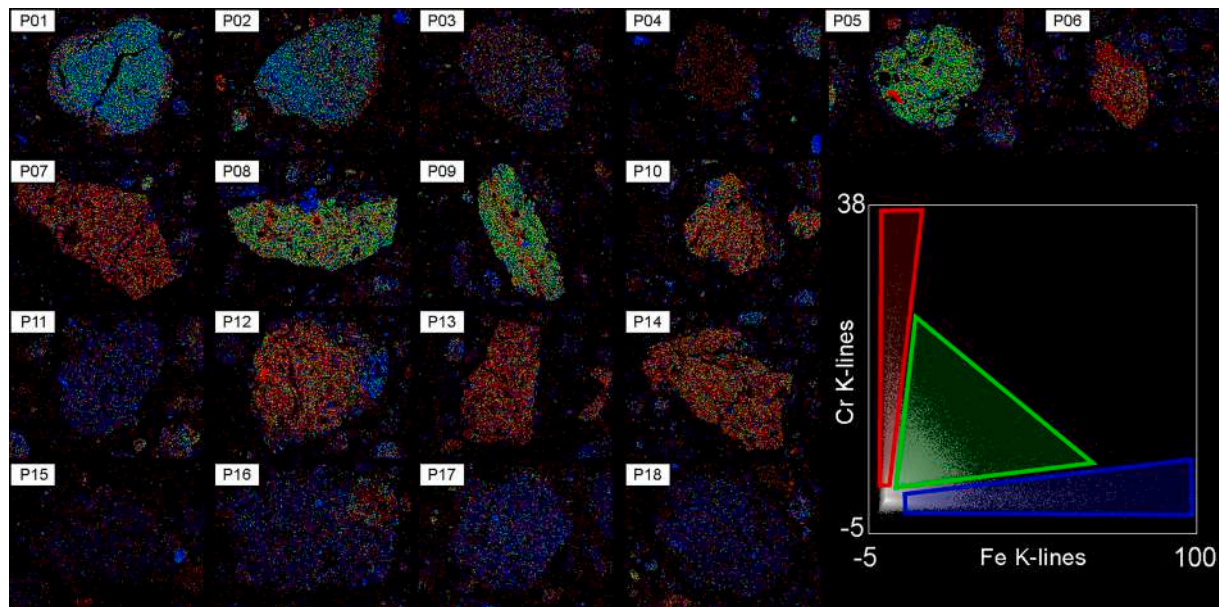It is remarkable that the application of spectral deconvolution in

Fig. 7. Identification of three different regions on the base of Fe vs Cr scatterplot (right graph) and their identification in the studied soil aggregates (small panels). The fitted net EDX intensities in the scatter biplots are expressed in counts.

hyperspectral data analysis of SEM-EDX data cubes allowed the identification of so many different features which, in turn, allowed the differentiation of soil aggregates having different chemical composition and origin. All this information, together with additional bulk soil analyses (e.g, determination of mineralogical composition, texture, soil chemical composition, basic soil chemical-physical properties, etc.) could contribute to identify the sources/causes of soil pollution and study related transformation processes that may occur over time.

4. Conclusions

The use of hyperspectral data analysis of SEM-EDX datacubes was applied to the characterization of soil aggregates by using a modified version of the software "Datamuncher Gamma". Datamuncher Gamma allows to get elemental distribution maps from hyperspectral datasets and compare the characteristic net EDX lines intensities of all the elements found in the sample. On top of this, it allows to create scatter biplots, based on the fitted net-intensities of two elemental lines. The visual recognition of correlations between elements allows the identification of specific mineral phases and soil features. Applying this method to the study of a single aggregate, a total of 9 phases were recognized (aluminosilicate matrix, quartz, K-feldspar, plagioclase, CaMg-aluminosilicate, Ca-carbonates, Ca-phosphates, Fe oxides and organic matter) and quantified. Of course, the precise mineralogical phase cannot be defined in the case of polymorph minerals (e.g. orthoclase, sanidine, microcline for K-feldspars) since the discrimination is done only on the basis of the elemental composition. In a second step, the method was used for the discrimination among soil aggregates with different composition, as well as to hypothesize the soil pedological history. Autochthone soil aggregates were mainly characterized by an aluminosilicate composition, while Cr-containing aggregates were of anthropic origin, mainly deriving from the disposal of organic tannery wastes on the studied site. However, among these allochthonous aggregates, differences were found according to their Cr/Fe ratio which might be due to different contamination sources or to the spreading of different wastes coming from the same production process or in different periods. This method, here applied to soil samples, can be used for SEM-EDX data analysis of any kind of sample characterized by both simple and complex matrixes. The main limit of this approach consists of the comparison of only two elements per time and, for this reason, a

principal components analysis (PCA) could be implemented in the software in order to consider more than two elements for a better and faster phase identification.

Declaration of Competing Interest

The authors declare that they have no known competing financial interests or personal relationships that could have appeared to influence the work reported in this paper.

Appendix A. Supplementary data

Supplementary data to this article can be found online at https://doi.org/10.1016/j.geoderma.2021.115540.

References

Alfeld, M., Janssens, K., 2015. Strategies for processing mega-pixel X-ray fluorescence hyperspectral data: a casu study on a version of Caravaggio's painting Supper at Emmaus. J. Anal. Atom. Spectrometry 30, 777–789. https://doi.org/10.1039/c4ja00387j.

Allegretta, I., Pinto, D., Eramo, G., 2016. Effects of the grain size on the reactivity of limestone temper in a kaolinitic clay. Appl. Clay Sci. 126, 223–234. https://doi.org/10.1016/j.clay.2016.03.020.

Allegretta, I., Porfido, C., Martin, M., Barberis, E., Terzano, R., Spagnuolo, M., 2018. Characterization of As-polluted soils by laboratory X-ray based techniques coupled with sequential extractions and electron microscopy: the case of Crocette gold mine in the Monte Rosa mining district (Italy). Environ. Sci. Pollut. R. 25 (25), 25080–25090. https://doi.org/10.1007/s11356-018-2526-9.

Astolfi, S., Pii, Y., Terzano, R., Mimmo, T., Celletti, S., Allegretta, I., Lafiandra, I., Cesco, S., 2018. Does Fe accumulation in durum wheat seeds benefit from improved

whole-plant sulfur nutrition? J. Cereal Sci. 83, 74–82. https://doi.org/10.1016/j.jcs.2018.07.010.

Baveye, P.C., Otten, W., Kravchenko, A., Balseiro-Romero, M., Beckers, E., Chalhoub, M., Darnault, C., Eickhorst, T., Garnier, P., Hapca, S., Kiranyaz, S., Monga, O., Mueller, C.W., Nunan, N., Pot, V., Schluter, S., Schmidt, H., Vogel, H.J., et al., 2018. Emergent properties of microbial activity in heterogeneous soil microenvironments: different research approaches are slowly converging, yet major challenges remain. Front. Microbiol. 9, 1–48. https://doi.org/10.3389/fmicb.2018.01929.

Burdet, P., Croxall, S.A., Midgley, P.A., 2015. Enhanced quantification for 3D SEM-EDS: using the full set of available X-ray lines. Ultramicroscopy 148, 158–167. https://doi.org/10.1016/j.ultramic.2014.10.010.

Cagno, S., Lind, O.C., Popic, J.M., Skipperud, L., De Nolf, W., Nuyts, G., Vanmeert, F., Jaroszewicz, J., Janssens, K., Salbu, B., 2020. Micro-analytical characterization of thorium-rich aggregates from Norwegian NORM sites (Fen Complex, Telemark). J. Envirn. Radioactiv. 219, 106273. https://doi.org/10.1016/j.jenvrad.2020.106273.

Carlton, R.A., 2010. Image analysis of EDS and Backscatter SEM Images of pharmaceutical tablets. Microsc. Microanal. 16 (S2), 662–663. https://doi.org/10.1017/S1431927610061283.

Chadwick, O.A., Chorover, J., 2001. The chemistry of pedogenic thresholds. Geoderma 100 (3-4), 321–353. https://doi.org/10.1016/S0016-7061(01)00027-1.

Ernst, T., Berman, T., Buscaglia, J., Eckert-Lumsdon, T., Hanlon, C., Olsson, K., Palenik, C., Pyland, S., Trejos, T., Valadez, M., Almirall, J.R., 2014. Signal-to-noise ratios in forensic glass analysis by micro X-ray fluorescence spectrometry. X-ray Spectrom. 43, 13–21. https://doi.org/10.1002/xrs.2437.

Falsone, G., Bonifacio, E., Zanini, E., 2012. Structure development in aggregates of poorly developed soils through the analysis of the pore system. Catena 95, 169–176. https://doi.org/10.1016/j.catena.2012.02.014.

Fela, K., Wieczorek-Ciurowa, K., Konopka, M., Woźny, Z., 2011. Present and prospective leather industry waste disposal. Pol. J. Chem. Technol. 13 (3), 53–55. https://doi.org/10.2478/v10026-011-0037-2.

Gattullo, C.E., D'Alessandro, C., Allegretta, I., Porfido, C., Spagnuolo, M., Terzano, R., 2018. Alkaline hydrothermal stabilization of Cr(VI) in soil using glass and aluminium from recycled municipal solid wastes. J. Hazard. Mater. 344, 381–389. https://doi.org/10.1016/j.jhazmat.2017.10.035.

Gattullo, C.E., Allegretta, I., Porfido, C., Rascio, I., Spagnuolo, M., Terzano, R., 2020. Assessing chromium pollution and natural stabilization processes in agricultural soils by bulk and micro X-ray analysis. Environ. Sci. Pollut. R. 27, 22967–22979. https://doi.org/10.1007/s11356-020-08857-3.

Gerke, K.M., Korostilev, E.V., Romanenko, K.A., Karsanina, M.V., 2021. Going submicron in the precise analysis of soil structure: a FIB-SEM imaging study at nanoscale. Geoderma 383, 114739. https://doi.org/10.1016/j.geoderma.2020.114739.

Germinario, L., Cossio, R., Maritan, L., Borchi, A., Mazzoli, C., 2016. Textural and mineralogical analysis of volcanic rocks by μ-XRF mapping. Microsc. Microanal. 22, 690–697. https://doi.org/10.1017/S1431927616000714.

Goldstein, J.I., Newbury, D.R., Michael, J.R., Ritchie, N.W.M., Scott, J.H.K., Joy, D.C., 2018. Scanning Electron Microscopy and X-ray Microanalysis, third ed. Springer, New York.

Hapca, S.M., Wang, Z.X., Otten, W., Wilson, C., Baveye, P.C., 2011. Automated statistical method to align 2D chemical maps with 3D X-ray computed micro-tomographic images of soils. Geoderma 164 (3-4), 146–154. https://doi.org/10.1016/j.geoderma.2011.05.018.

Hapca, S., Baveye, P.C., Wilson, C., Lark, R.M., Otten, W., Singer, A.C., 2015. Three-dimensional mapping of soil chemical characteristics at micrometric scale by combining 2D SEM-EDX data and 3D X-ray CT images. Plos One 10 (9), e0137205. https://doi.org/10.1371/journal.pone.0137205.

Kannaujiya, M.C., Mandal, T., Mandal, D., Mondal, M.K., 2019. Treatment of leather industry wastewater and recovery of valuable substances to solve waste management problem in environment. In: Bharagava, R.N. (Ed.), Environmental contaminants: ecological implications and management. Springer Nature Singapore, Singapore, pp. 311–340.

Kenda, A., Eibl, O., Pongratz, P., 1999. Multiphase analysis with EDX elemental maps: software implementation and application to (Bi, Pb)2Sr2Ca2Cu3O10+δ. Micron 30, 85–97. https://doi.org/10.1016/S0968-4328(98)00033-X.

Kotula, P.G., Keenan, M.R., 2003. Automated analysis of SEM X-ray spectral images: a powerful new microanalysis tool. Microsc. Microanal. 9 (1), 1–17. https://doi.org/10.1017/S1431927603030058.

Legrand, S., Van der Snickt, G., Cagno, S., Caen, J., Janssens, K., 2019. MA-XRF imaging as a tool to characterize the 16th century heraldic stained-glass panel in Ghent Sint Bavo Cathedral. J. Cult. Herit. 40, 163–168. https://doi.org/10.1016/j.culher.2019.06.003.

Li, Q., Hu, X., Hao, J., Chen, W., Cai, P., Huang, Q., 2020. Characterization of Cu distribution on clay-sized soil aggregates by NanoSIMS and micro-XRF. Chemosphere 249, 126143. https://doi.org/10.1016/j.chemosphere.2020.126143.

Lin, H., 2011. Three principles of soil change and pedogenesis in time and space. Soil Sci. Soc. Am. J. 75 (6), 2049–2070. https://doi.org/10.2136/sssaj2011.0130.

Lu, Y., Luo, D., Lai, A.n., Liu, G., Liu, L., Long, J., Zhang, H., Chen, Y., 2017. Leaching characteristics of EDTA-enhanced phytoextraction of Cd and Pb by Zea mays L., in different particle-size fractions of soil aggregates exposed to artificial rain. Environ. Sci. Pollut. Res. 24 (2), 1845–1853. https://doi.org/10.1007/s11356-016-7972-7.

Newbury, D.E., Ritchie, N.W.M., 2015. Performing elemental microanalysis with high accuracy and high precision by scanning electron microscopy/silicon drift detector energy-dispersive X-ray spectrometry (SEM/SDD-EDS). J. Mat. Sci. 50 (2), 493–518. https://doi.org/10.1007/s10853-014-8685-2.

Ozgunay, H., Colak, S., Mutlu, M.M., Akyuz, F., 2007. Characterization of leather industy wastes. Polish J. Environ. Stud. 16, 867–873.

Porfido, C., Allegretta, I., Panzarino, O., Laforce, B., Vekemans, B., Vincze, L., de Lillo, E., Terzano, R., Spagnuolo, M., 2019. Correlation between As in earthworms' coelomic fluid and As bioavailability in highly polluted soils as revealed by combined laboratory X-ray techniques. Environ. Sci. Technol. 53, 10961–10968. https://doi.org/10.1021/acs.est.9b02310.

Rillig, M.C., Muller, L.AH., Lehmann, A., 2017. Soil aggregates as massively concurrent evolutionary incubators. ISME J. 11 (9), 1943–1948. https://doi.org/10.1038/ismej.2017.56.

Roduit, N., 2007. JMicroVision: un logiciel d'analyse d'images pétrographiques polyvalent, Ph.D. Thesis. Université de Genève. 10.13097/archive-ouverte/unige: 468.

Ryan, C.G., Jamieson, D.N., 1993. Dynamic analysis: on-line quantitative PIXE microanalysis and its use in overlap-resolved elemental mapping. Nucl. Instrum. Meth. B 77 (1-4), 203–214. https://doi.org/10.1016/0168-583X(93)95545-G.

Schlüter, S., Eickhorst, T., Mueller, C.W., 2019. Correlative imaging reveal holistic view of soil microenvironments. Environ. Sci. Technol. 53, 829–837. https://doi.org/10.1021/acs.est.8b05245.

Silva, M.D.M., Barajas-Aceves, M., Araujo, A.S.F., Araujo, F.F., Melo, W.J., 2014. Soil microbial biomass after three-year consecutive composted tannary sludge amendment. Pedosphere 24, 269–475. https://doi.org/10.1016/S1002-0160(14)60033-3.

Solé, V.A., Papillon, E., Cotte, M., Walter, P.h., Susini, J., 2007. A multiplatform code for the analysis of energy-dispersive X-ray fluorescence spectra. Spectrochim. Acta B 62 (1), 63–68.

Tokunaga, T.K., Wan, J., Hazen, T.C., Schwartz, E., Firestone, M.K., Sutton, S.R., Newville, M., Olson, K.R., Lanzirotti, A., Rao, W., 2003. Distribution of chromium contamination and microbial activity in soil aggregates. J. Environ. Qual. 32 (2), 541–549. https://doi.org/10.2134/jeq2003.5410.

Tokunaga, T.K., Wan, J., Firestone, M.K., Hazen, T.C., Schwartz, E., Sutton, S.R., Newville, M., 2001. Chromium diffusion and reduction in soil aggregates. Environ. Sci. Technol. 35 (15), 3169–3174. https://doi.org/10.1021/es010523m.

Van der Snickt, G., Legrand, S., Caen, J., Vanmeert, F., Alfeld, M., Janssens, K., 2016. Chemical imaging of stained-glass windows by means of macro X-ray fluorescence (MA-XRF) scanning. Microchem. J. 124, 615–622. https://doi.org/10.1016/j.microc.2015.10.010.

Van Espen, P., 2002. Spectrum evaluation. In: van Grieken, R., Markowicz, A. (Eds.), Handbook of x-ray spectrometry. Marcel Dekker Inc., New York, pp. 239–340.

Vazquez, M.A., Galan, E., Ortiz, P., Ortiz, R., 2013. Digital image analysis and EDX SEM as combined techniques to evaluate salt damp on walls. Constr. Build. Mater. 45, 95–105. https://doi.org/10.1016/j.conbuildmat.2013.03.067.

Wells, O.C., 2001. Scanning Electron Microscopy. In: Buschow, K.H.J., Cahn, R.W., Flemings, M.C., Ilschner, B., Kramer, E.J., Mahajan, S., Veyssière, P. (Eds.), Encyclopedia of Materials: Science and Technology. Elsevier, Amsterdam, New York.

Zhong, S., Wei, C., Ni, J., Xie, D., Ni, C., 2020. Characterization of clay rock-derived soils containing multi-mineral sand particles in upland areas of Sichuan Basin, China. Catena 194, 104737. https://doi.org/10.1016/j.catena.2020.104737.